Supporting Information

Zhi-Heng Zhou[+],[a,b] Xiao-Bo Li[+],[a] Zhi-Wei Huang,[a] Qun-Yan Wu,[a] Jun-Xi Wang,[a,b] Zhi-Hui Zhang,[c] Lei Mei,[a] Fu-Qiu Ma,*[b] Kong-Qiu Hu,*[a] and Wei-Qun Shi*[a]

[a] Laboratory of Nuclear Energy Chemistry, Institute of High Energy Physics, Chinese Academy of Sciences, Beijing, 100049, China.

[b] Yantai Research Institute, Harbin Engineering University, Yantai, 264006, Shandong, China.

[c] Jiangsu Key Laboratory of Advanced Catalytic Materials and Technology, Advanced Catalysis and Green Manufacturing Collaborative Innovation Center, Changzhou University, Changzhou, 213164 China.

[+] These authors contribute equally: Zhi-Heng Zhou, Xiao-Bo Li.

Synthesis

5-methoxy-4-hydroxybenzoic acid (16.1 mmol) was dissolved in trifluoroacetic acid (15 mL) under a nitrogen atmosphere (Scheme S1). A solution of hexamethylenetetramine (33.0 mmol) in trifluoroacetic acid (25 mL) was added dropwise to this solution. The mixture was heated at reflux for 24 h. After cooling to room temperature, 3 M HCl solution (200 mL) was added to the clear orange solution, from which a beige solid precipitated. The solid was filtered, washed with water, and air-dried yielding 3-formyl-4-hydroxy-5-methoxybenzoic acid. ^{1}H NMR (500 MHz, DMSO-d_6.) δ = 12.94 (s, 1H), 10.99 (s, 1H), 10.31 (s, 1H), 7.89-7.88 (d, J =5 Hz ,1H), 7.65-7.64 (d, J =5 Hz, 1H), 3.91 (s, 3H).

3-formyl-4-hydroxy-5-methoxybenzoic acid (10 mmol) was dissolved in methanol (50mL), and added 2,2-dimethyl-1,3-propanediamine (5 mmol) into the solution, stirring at room temperature for 5h (Scheme S1). The solid was filtered, washed with methanol, and air-dried yielding H₄L1. ^{1}H NMR (500 MHz, DMSO-d_6.) δ = 8.65 (s, 1H), 7.70 (s, 1H), 7.37 (s, 1H), 3.79 (s, 3H), 3.53 (s, 2H), 1.01 (s, 3H).

3-formyl-4-hydroxy-5-methoxybenzoic acid (10 mmol) was dissolved in methanol (50mL), and added ethylenediamine (5 mmol) into the solution, stirring at room temperature for 5h (Scheme S2). The solid was filtered, washed with methanol, and air-

dried yielding H$_4$L2. ^{1}H NMR (500 MHz, DMSO-d$_6$.) δ = 8.64 (s, 1H), 7.65 (s, 1H), 7.38 (s, 1H), 3.95 (s, 2H), 3.77 (s, 3H).
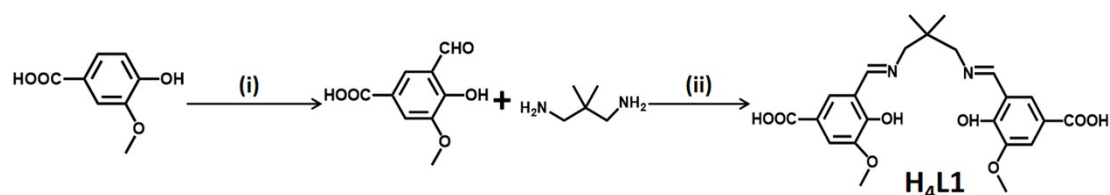
Scheme S1. Synthetic method of Schiff base ligand H$_4$L1; (i) CF$_3$COOH, hexamethylenetetramine (2 equiv.), reflux, 24 h; (ii) EtOH, 2, 2-dimethyl-1, 3-propanediamine (0.5 equiv.), stir, 5 h;
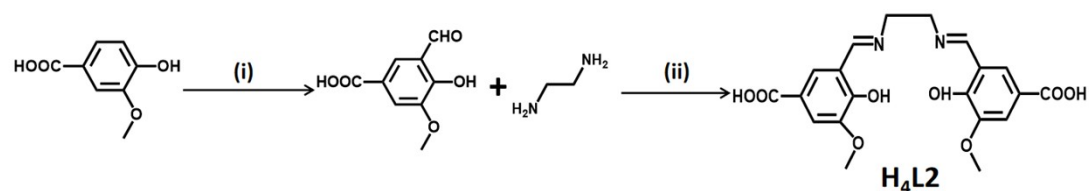
Scheme S2. Synthetic method of Schiff base ligand H$_4$L2; (i) CF$_3$COOH, hexamethylenetetramine (2 equiv.), reflux, 24 h; (ii) EtOH, ethylenediamine (0.5 equiv.), stir, 5 h;

Characterization

Single crystal X-ray data of IHEP-101 and IHEP-102 were collected on a Bruker APEXII X-ray diffractometer equipped with a CMOS PHOTON 100 detector with a MoKα X-ray source (Kα= 0.71073 Å). Data were indexed, integrated, and scaled using SAINT v8.37A (Bruker, 2015). The structures were solved by direct method (SHELXS-97, Sheldrick 2008) and refined by full-matrix least-squares (SHELXL 2018/3, Sheldrick, 2015) on F^2. Anisotropic thermal parameters were used for the non-hydrogen atoms and isotropic parameters for the hydrogen atoms. The SQUEEZE routine of PLATON was used to remove the diffraction contribution from disordered solvents of compound. A summary of crystal parameters and structure refinement are provided in Table S1. Selected bond distances and angles are listed in Table S2 and Table S3. Powder X-ray diffraction (PXRD) patterns were collected on a Bruker D8 Advance X-ray diffractometer with Cu Kα radiation (λ=1.5406 Å). The accelerating

voltage and the applied current were 40 kV and 40 mA, respectively. Data were recorded in the 2θ range from 3° to 50°. Simulated PXRD patterns were obtained from SCXRD data using Mercury 3.3 software from the Cambridge Crystal Data Center (CCDC). The Fourier transform infrared (FT-IR) spectra were recorded on a Bruker Tensor 27 infrared spectrometer. Sample was diluted with spectroscopic KBr and pressed into a pellet. The measured wavenumber is between 400 and 4000 cm^{-1}. Thermogravimetric analysis (TGA) was performed on a TA Q500 analyzer over the temperature range of 30-800 °C in an air atmosphere with a heating rate of 5 °C min^{-1}. The N_2 and CO_2 adsorption/desorption experiments were measured on a micromeritics ASAP 2460 apparatus at liquid nitrogen temperature (-196 °C) and RT, respectively. Thermogravimetric analysis (TGA) was performed on a TA Q500 analyzer over the temperature range of 30-800 °C in an air atmosphere with a heating rate of 5 °C/min. SEM images were obtained by a FEI Quanta FEG 250 instruments at the accelerating voltage of 20 kV.

Photocatalytic CO_2 Reduction

In a typical photocatalytic CO_2 reduction experiment, 5 mg MOF sample and 5 mg $[Ru(bpy)_3]Cl_2 \cdot 6H_2O$ were suspended in a mixed solution of 4 mL CH_3CN and 1 mL H_2O, placed in a custom-made 20 mL photocatalytic reaction cell, degassed and saturated with CO_2 (purity > 99.999%) for 0.5 h to remove any dissolved impurity gases, then seal the reaction cell. The reaction was carried out under the irradiation of a 300 W Xe lamp (CEL-PE300L-3A) equipped with 420 nm cut-off filter. Gas chromatography (GC-7920) was applied to analyzed possible gaseous products (H_2, CO, CH_4) by the detectors of a thermal conductivity detector (TCD) and a flame ionization detector (FID) using Ar as the carrier gas. The amount of possible liquid products (CH_3OH, CH_3COOH) was detected by ^{1}H NMR spectra on a Bruker Avance III 500 MHz spectrometer. Specifically, 500 μL of solution after photocatalysis were mixed with 100 μL D_2O and 0.05 μL dimethyl sulfoxide as internal standard.

Computational Methods

All calculations were performed by using B3LYP hybrid functional[1, 2] in the Gaussian

16 program, as used previously for calculating actinide complexes[3-5]. The relativistic effective core potential (RECP)[6] using the 60 core electrons combined with the ECP60MWB-SEG valence basis set[7, 8] was employed for U and the 6-31G(d) basis set was applied to C, N, O, and H. The solvation model density (SMD)[9] was used to simulate the reaction environment by using n,n-dimethylformamide (DMF) as solvent. Gibbs free energies were used for the reported potential energy profile (PEP). Calculations of harmonic vibrational frequencies were implemented to ensure only negative value for the structure of the transition state (TS) and positive value for the other optimized structures. Intrinsic reaction coordinate (IRC) calculations confirm that the initial complex (IC) is connected to the intermediate (INT) via the TS. Spin density analysis was performed to elucidate the transformation of the U atomic oxidation state on the PEPs using the Multiwfn code.[10]

Table S1. Crystallographic Data and Structure Refinement Results.

	IHEP-101	IHEP-102
Formula	$C_{124}H_{203}N_{25}O_{52}U_5$	$C_{26}H_{30}N_4O_{14}U_2$
Formula weight	4066.25	1098.60
CCDC	2358409	2358410
Crystal system	monoclinic	monoclinic
space group	$C2/c$	$P2_1/c$
a (Å)	45.847(6)	17.9735(15)
b (Å)	29.165(4)	14.9023(13)
c (Å)	14.8586(17)	12.2543(9)
α (deg)	90	90
β (deg)	107.195(4)	96.152(3)
γ (deg)	90	90
V (Å³)	18980(4)	3263.4(5)
Z	4	4
Temperature (K)	170	170

λ	0.71073	0.71073
ρ(calc) g/cm^3	1.423	2.236
F (000)	7992	2040
μ (mm^{-1})	4.325	9.984
R_{int}	0.0945	0.087
GOF on F^2	1.043	1.043
R_1^a/wR$_2^b$[I>2σ(I)]	0.0483/0.1271	0.0290/0.0702

$^aR_1=\sum (F_o - F_c)/\sum F_o$; $^bwR_2=[\sum w(F_o^2 - F_c^2)^2/\sum w(F_o^2)^2]^{1/2}$.

Table S2 Selected Bond Distances (Å) of IHEP-101

Atoms	Length/Å	Atoms	Length/Å	Atoms	Length/Å
U(1)-O(1)	2.284(12)	U(2)-O(9)	1.760(12)	U(2)-O(00D)	2.475(10)
U(1)-O(2)	2.273(12)	U(2)-O(10)	1.776(8)	U(3)-O(5)	2.229(12)
U(1)-O(7)	1.750(13)	U(2)-O(004)	2.509(10)	U(3)-O(11)	1.737(13)
U(1)-O(8)	1.774(8)	U(2)-O(005)	2.491(9)	U(3)-O(15)	2.40(2)
U(1)-O(12)	2.399(13)	U(2)-O(006)	2.450(10)	U(3)-N(3)	2.512(14)
U(1)-N(1)	2.559(14)	U(2)-O(009)	2.446(10)		
U(1)-N(2)	2.612(15)	U(2)-O(00B)	2.385(10)		

Table S3 Selected Bond Distances (Å) of IHEP-102

Atoms	Length/Å	Atoms	Length/Å	Atoms	Length/Å
U(1)-O(1)	1.770(7)	U(1)-N(1)	2.577(7)	U(2)-O(10)	2.431(7)
U(1)-O(2)	1.776(6)	U(1)-N(2)	2.553(7)	U(2)-O(11)	2.349(7)
U(1)-O(5)	2.254(6)	U(2)-O(3)	1.719(7)	U(2)-O(12)	2.274(8)
U(1)-O(6)	2.270(6)	U(2)-O(4)	1.765(8)	U(2)-O(14)	2.374(10)
U(1)-O(13)	2.351(7)	U(2)-O(9)	2.465(7)		

Table S4. Activity comparison of recently reported MOF photocatalysts for CO$_2$

reduction.

Photocatalyst	Solvent	Light source	Photosensitizer	Sacrificial agent	Major Products	CO Generation Rate ($\mu mol\ g^{-1}\ h^{-1}$)	CO Selectivity	References
IHEP-20	CH$_3$CN	300 W Xe lamp	-	TEOA	CO, CH$_4$	297	95.3%	11
POMs@IHEP-20						970	97.1%	
MOF-525-Co	CH$_3$CN	300 W Xe lamp	-	TEOA	CO, CH$_4$	201.6	84.6%	12
MOF-525-Zn						111.7	91.6%	
MOF-525						64.02	91.2%	
Co-MOF-3	H$_2$O	300 W Xe lamp	[Ru(bpy)$_3$] Cl$_2$	TEOA	CO	27.1	100%	13
Ni3@Ru-UiO-67	DMF/H$_2$O	82 W LED light	-	TEOA, BIH	CO	426.05	99%	14
Co-ZIF-67	CH$_3$CN/H$_2$O	300 W Xe lamp	[Ru(bpy)$_3$] Cl$_2$	TEOA	CO, H$_2$	59200	66.7%	15
PCN-222	-	300 W Xe lamp	-	-	CO, CH$_4$	5.5	61.1%	16
PCN-601						6.0	37.3%	
MOF-808-CuNi	CH$_3$CN	300 W Xe lamp	[Ru(bpy)$_3$] Cl$_2$	TEOA	CO, CH$_4$, HCOOH, H$_2$	2.3	1.4%	17
MOF-808-Cu						4.2	6%	
Au-NC@UiO-68-NHC	CH$_3$CN	300 W Xe lamp	-	MeOH	CO, CH$_4$, H$_2$	57.6	97%	18
UiO-68-NHC						2.7	97.2%	
UiO-68-NH2/Au						13.4	97.3%	
BIF-20@g-C3N4	CH$_3$CN	300 W Xe lamp	-	TEOA	CO, CH$_4$	53.869	77.6%	19
P25/Ti3C2 MXene	-	300 W Xe lamp	-	H$_2$O	CO, CH$_4$	12.6	88.7%	20
IHEP-101	CH$_3$CN	300 W Xe lamp	[Ru(bpy)$_3$] Cl$_2$	H$_2$O	CO, CH$_4$	458	98.6%	This work

Table S5. Calculated changes in the Gibbs free energies (eV) for reduction reaction of CO_2 to CO by IHEP-101.

Reaction	$\Delta E(eV)$
$[U(V)L1]^+ + CO_2 \rightarrow {}^*CO_2$	+1.33
${}^*CO_2 + H^+ \rightarrow {}^*COOH$	-1.05
${}^*COOH + H^+ \rightarrow {}^*CO + H_2O$	+3.34
${}^*CO \rightarrow [U(VI)L1]^{2+} + CO$	-0.47
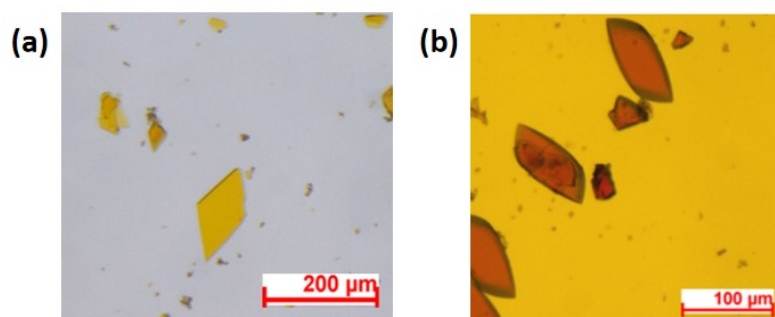
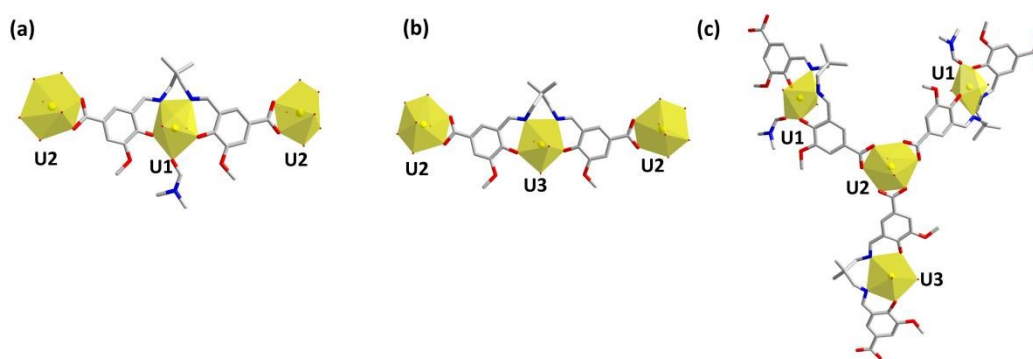Figure S1. The morphology of (a) IHEP-101 and (b) IHEP-102 under optical microscope.

Figure S2. (a, b) In IHEP-101, a $[UO_2(L1)]^{2-}$ ligand is connected to two UO_2^{2+} nodes and one DMF molecule or H_2O molecule. (c) The UO_2^{2+} node is connected to three $[UO_2(L1)]^{2-}$ ligands. Color scheme: U, yellow; C, gray; O, red; N, blue. Hydrogen atoms were omitted for clarity.
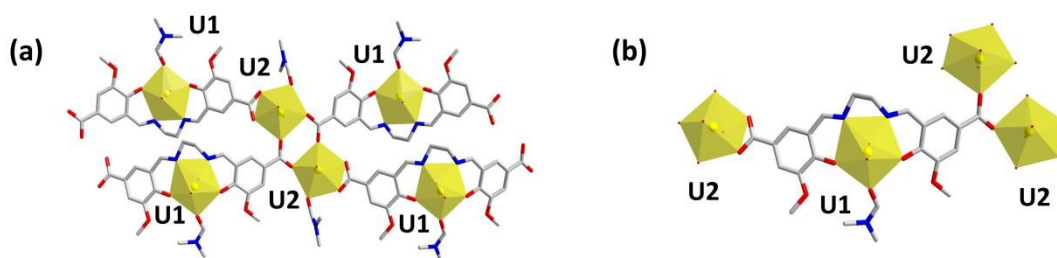
Figure S3. (a) In IHEP-102, two UO_2^{2+} nodes is connected to four $[UO_2(L2)]^{2-}$ ligands and two DMF molecules. (b) The $[UO_2(L2)]^{2-}$ ligand is connected to three UO_2^{2+} nodes and one DMF molecule. Color scheme: U, yellow; C, gray; O, red; N, blue. Hydrogen atoms were omitted for clarity.
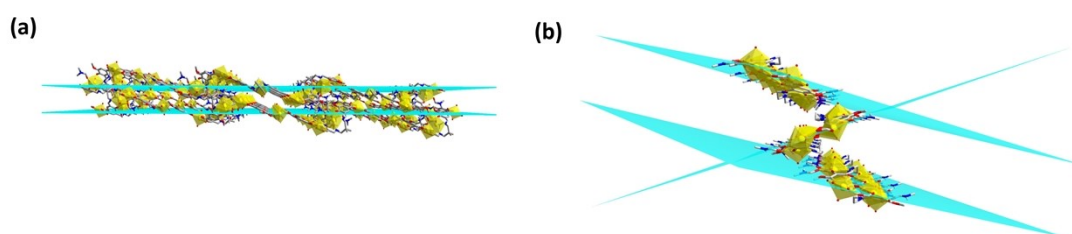

Figure S4. (a) Interlayer stacking of IHEP-101. (b) Interchain stacking of IHEP-102. Color scheme: U, yellow; C, gray; O, red; N, blue. Hydrogen atoms were omitted for clarity.
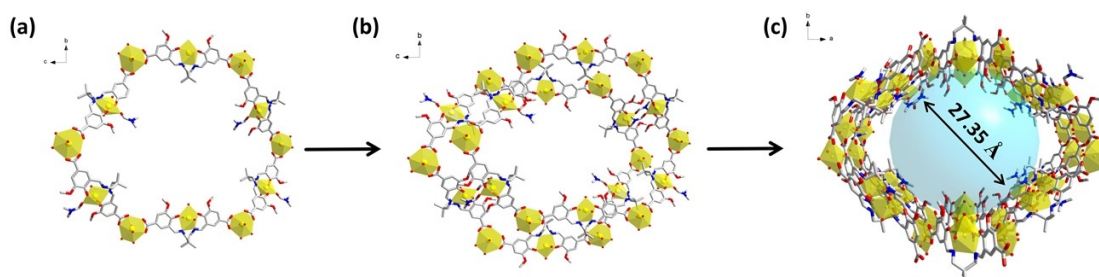
Figure S5. Pore structure of IHEP-101 changes due to interlayer accumulation. Color scheme: U, yellow; C, gray; O, red; N, blue. Hydrogen atoms were omitted for clarity.
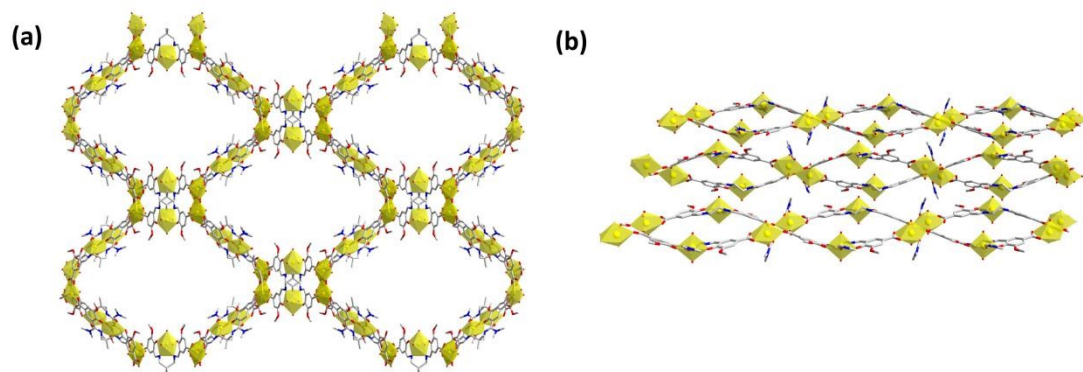
Figure S6. (a) The complete structure of IHEP-101. (b) The complete structure of IHEP-102. Color scheme: U, yellow; C, gray; O, red; N, blue. Hydrogen atoms were omitted for clarity.
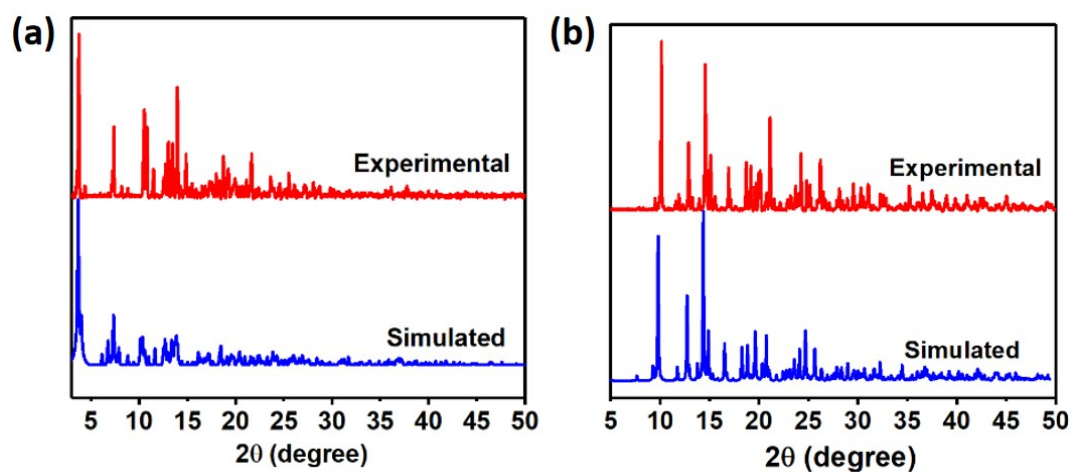
Figure S7. The PXRD patterns of (a) IHEP-101 and (b) IHEP-102.
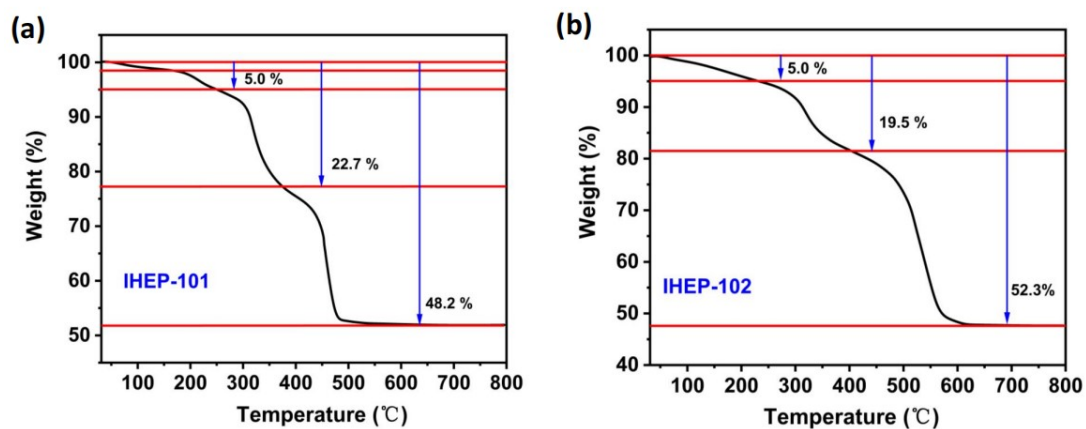
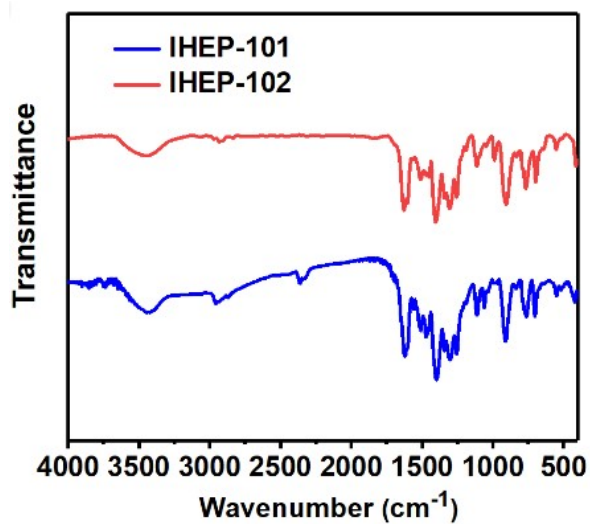Figure S8. TGA of (a) IHEP-101 and (b) IHEP-102 measured under an air atmosphere.

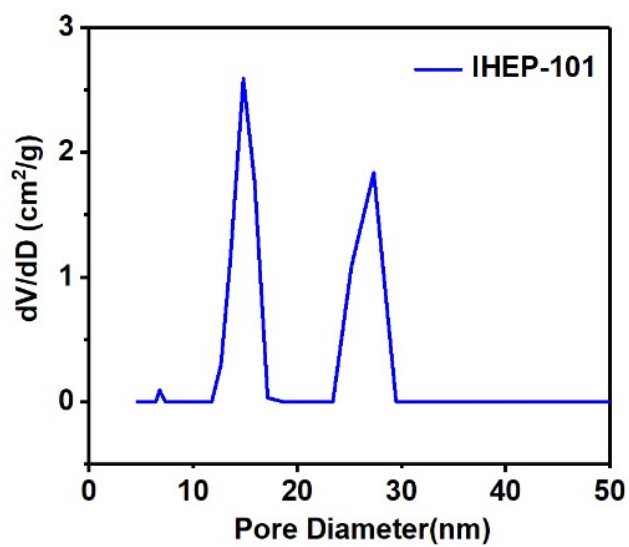Figure S9. The IR spectra of IHEP-101 and IHEP-102.
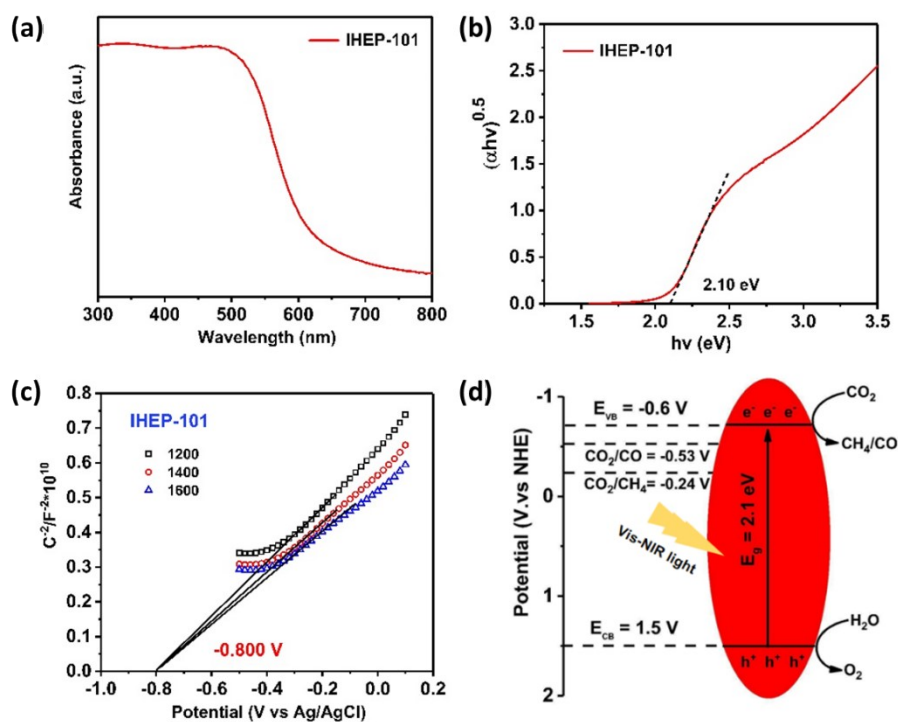

Figure S10. The pore size distribution of IHEP-101.

Figure S11. (a) The UV-Vis DRS spectrum of IHEP-101. (b) The corresponding plots of the (ahv)$^{0.5}$ versus photon energy (hv) for IHEP-101. (c) The Mott-Schottky plot of IHEP-101. (d) The energy level diagram of IHEP-101.

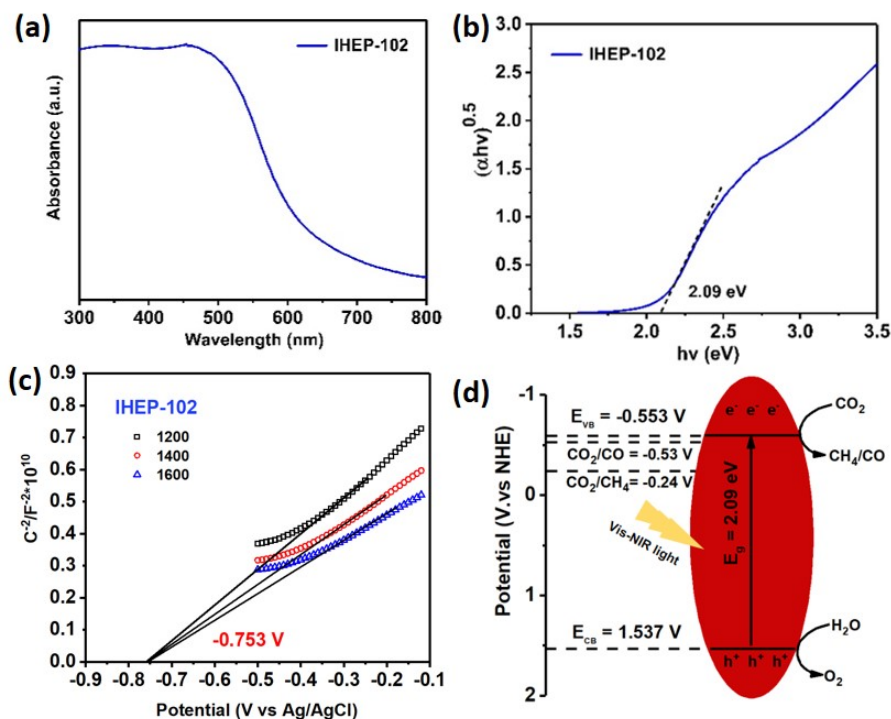Figure S12. (a) The UV-Vis DRS spectrum of IHEP-102. (b) The corresponding plots of the (ahv)$^{0.5}$ versus photon energy (hv) for IHEP-102. (c) The Mott-Schottky plot of IHEP-102. (d) The energy level diagram of IHEP-102.
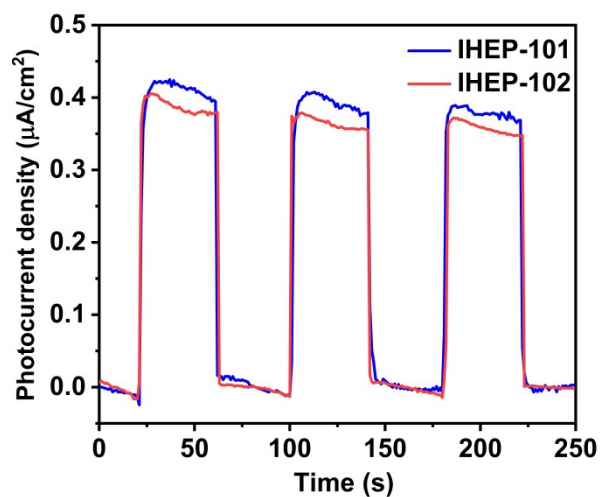
Figure S13. Transient photocurrent responses of IHEP-101 and IHEP-102 in 0.1 M Na$_2$SO$_4$ solution under 300W xenon light irradiation.
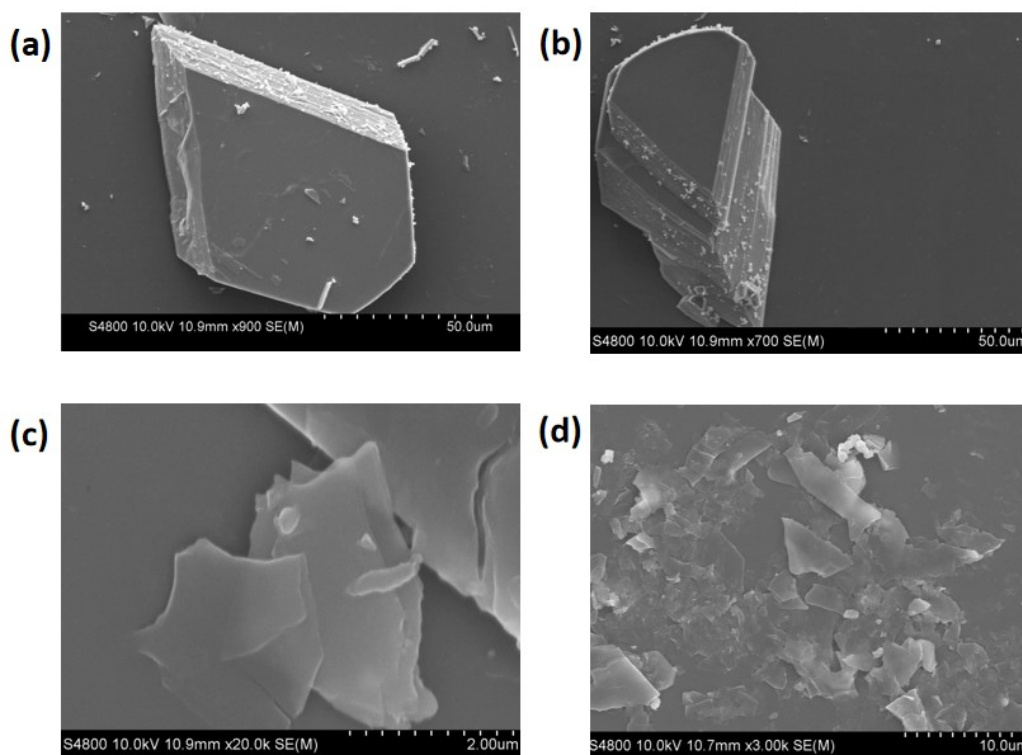

Figure S14. (a, b) The SEM spectra of IHEP-101 before catalysis. (c, d) The SEM spectra of IHEP-101 after photocatalysis.
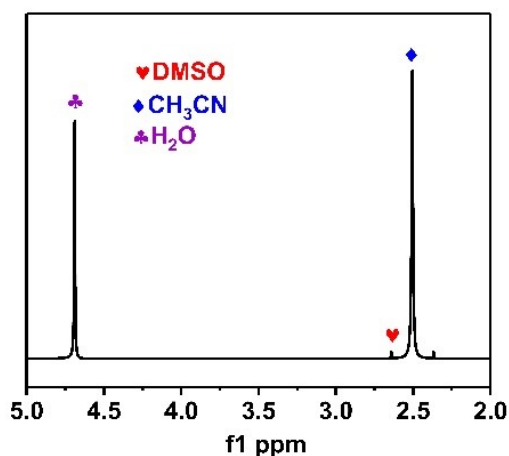
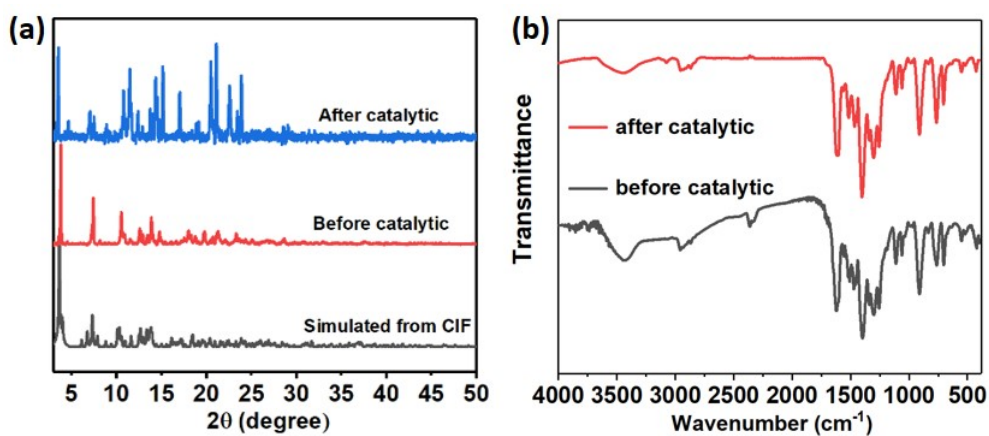Figure S15. The ^{1}H NMR spectrum of the liquid reaction products.

Figure S16. (a) The PXRD patterns of IHEP-101 before and after photocatalysis. (b) The IR spectra of IHEP-101 before and after photocatalysis.
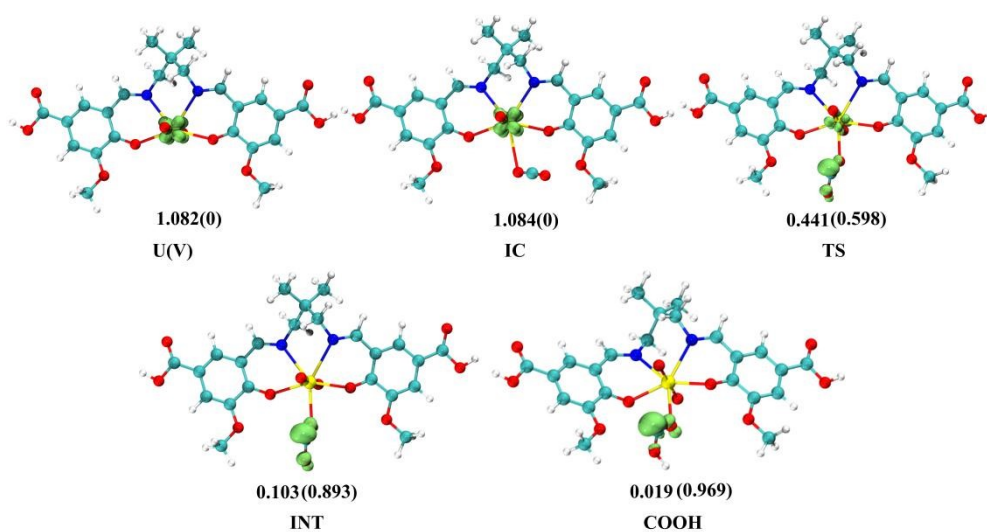

Figure S17. The spin density diagram for the CO_2 activation by IHEP-101. The value of spin density on the U atom and CO_2 fragment (in parenthesis).
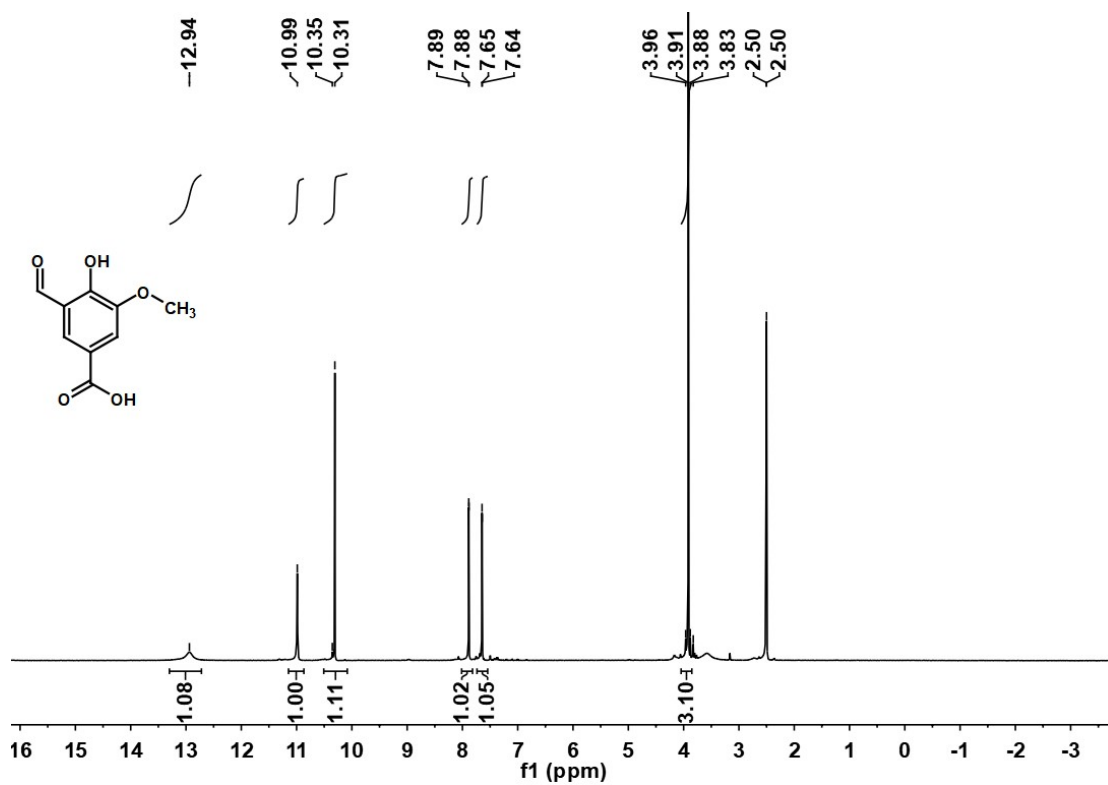
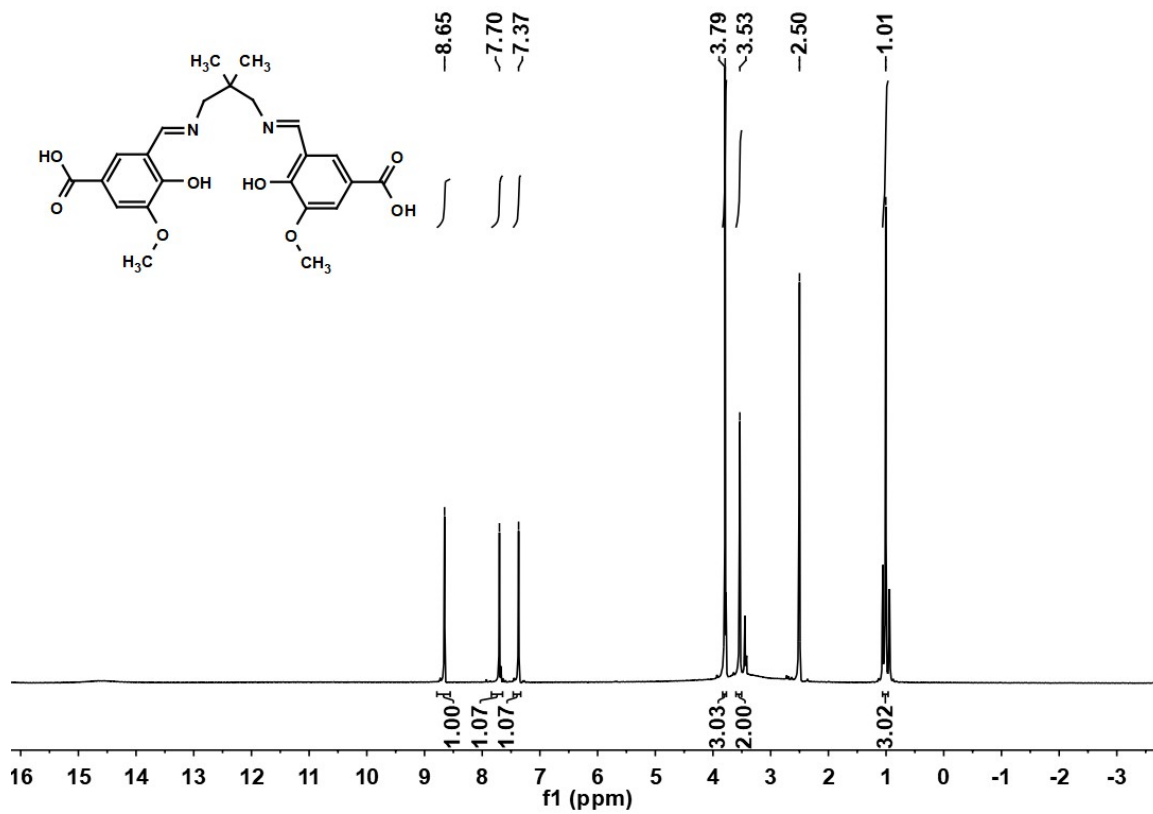Figure S18. ^{1}H NMR of 3-formyl-4-hydroxy-5-methoxybenzoic acid.
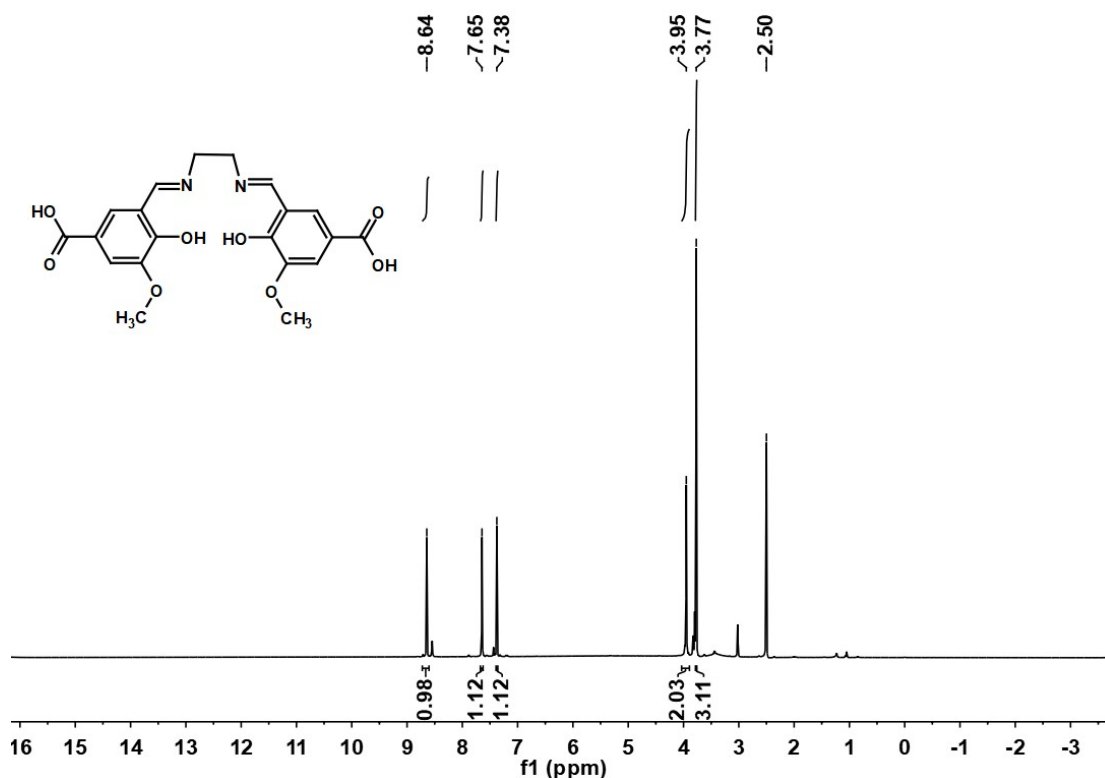
Figure S19. ^{1}H NMR of H$_4$L1.

Figure S20. ^{1}H NMR of H$_4$L2.

References

1. C. T. Lee, W. T. Yang and R. G. Parr, Development of the Colle-Salvetti Correlation-energy Formula Into a Functional of the Electron Density, *Phys. Rev. B*, 1988, **37**, 785-789.

2. A. D. Becke, Density-functional Thermochemistry. III. The Role of Exact Exchange, *J. Chem. Phys*, 1993, **98**, 5648-5652.

3. X. B. Li, Q. Y. Wu, C. Z. Wang, J. H. Lan, M. Zhang, Z. F. Chai and W. Q. Shi, Unveiling the Reduction Mechanism of Pu(IV) by Acetaldoxime, *J. Phys. Chem. A*, 2023, **127**, 7479-7486.

4. X. B. Li, Q. Y. Wu, C. Z. Wang, J. H. Lan, M. Zhang, Z. F. Chai and W. Q. Shi, Insights into the Reduction Mechanisms of Np(VI) to Np(V) by Carbohydrazide, *J. Phys. Chem. A*, 2023, **127**, 4259-4268.

5. Q. Y. Wu, J. H. Lan, C. Z. Wang, Y. L. Zhao, Z. F. Chai and W. Q. Shi, Understanding the Interactions of Neptunium and Plutonium Ions with Graphene Oxide: Scalar-Relativistic DFT Investigations, *J. Phys. Chem. A*, 2014, **118**, 10273-10280.

6. W. Kuchle, M. Dolg, H. Stoll and H. Preuss, Energy-adjusted Pseudopotentials for the Actinides-Parameter Sets and Test Calculations for Thorium and Thorium Monoxide, *J. Chem. Phys.*, 1994, **100**, 7535-7542.

7.   X. Y. Cao and M. Dolg, Segmented contraction scheme for small-core actinide pseudopotential basis sets, *J. Mol. Struct.: THEOCHEM*, 2004, **673**, 203-209.

8.   X. Y. Cao, M. Dolg and H. Stoll, Valence basis sets for relativistic energy-consistent small-core actinide pseudopotentials, *J. Chem. Phys*, 2003, **118**, 487-496.

9.   A. V. Marenich, C. J. Cramer and D. G. Truhlar, Universal Solvation Model Based on Solute Electron Density and on a Continuum Model of the Solvent Defined by the Bulk Dielectric Constant and Atomic Surface Tensions, *J. Phys. Chem. B*, 2009, **113**, 6378-6396.

10.   T. Lu and F. W. Chen, Multiwfn: A multifunctional wavefunction analyzer, *J. Comput. Chem*, 2012, **33**, 580-592.

11.   Z.-W. Huang, K.-Q. Hu, L. Mei, D.-G. Wang, J.-Y. Wang, W.-S. Wu, Z.-F. Chai and W.-Q. Shi, Encapsulation of Polymetallic Oxygen Clusters in a Mesoporous/Microporous Thorium-Based Porphyrin Metal–Organic Framework for Enhanced Photocatalytic CO_2 Reduction, *Inorg. Chem.*, 2022, **61**, 3368-3373.

12.   N. N. Wang, X. J. Xu, H. Y. Li, J. L. Zhai, L. Z. Yuan, K. X. Zhang and H. W. Yu, Preparation and Application of a Xanthate-Modified Thiourea Chitosan Sponge for the Removal of Pb(II) from Aqueous Solutions, *Ind. Eng. Chem. Res.*, 2016, **55**, 4960-4968.

13.   Y. N. Liu, C. S. Chen, J. Valdez, D. M. Meira, W. T. He, Y. Wang, C. Harnagea, Q. Q. Lu, T. Guner, H. Wang, C. H. Liu, Q. Z. Zhang, S. Y. Huang, A. Yurtsever, M. Chaker and D. L. Ma, Phase-enabled metal-organic framework homojunction for highly selective CO_2 photoreduction, *Nat. Commun.*, 2021, **12**, 1231.

14.   Q. Q. Ouyang, T. T. Hou, C. P. Li, Z. Hu, L. M. Liang, S. D. Li, Q. K. Zhong and P. W. Li, Construction of a composite sponge containing tilapia peptides and chitosan with improved hemostatic performance, *Int. J. Biol. Macromol.*, 2019, **139**, 719-729.

15.   J. N. Qin, S. B. Wang and X. C. Wang, Visible-light reduction CO_2 with dodecahedral zeolitic imidazolate framework ZIF-67 as an efficient co-catalyst, *Appl. Catal., B*, 2017, **209**, 476-482.

16.   Z. B. Fang, T. T. Liu, J. X. Liu, S. Y. Jin, X. P. Wu, X. Q. Gong, K. C. Wang, Q. Yin, T. F. Liu, R. Cao and H. C. Zhou, Boosting Interfacial Charge-Transfer Kinetics for Efficient Overall CO_2 Photoreduction via Rational Design of Coordination Spheres on Metal-Organic Frameworks, *J. Am. Chem. Soc.*, 2020, **142**, 12515-12523.

17.   J. Li, H. L. Huang, W. J. Xue, K. Sun, X. H. Song, C. R. Wu, L. Nie, Y. Li, C. Y. Liu, Y. Pan, H. L. Jiang, D. H. Mei and C. L. Zhong, Self-adaptive dual-metal-site pairs in metal-organic frameworks for selective CO_2 photoreduction to CH_4, *Nat. Catal.*, 2021, **4**, 719-729.

18.   Y. Jiang, Y. Yu, X. Zhang, M. Weinert, X. Song, J. Ai, L. Han and H. Fei, N-Heterocyclic Carbene-Stabilized Ultrasmall Gold Nanoclusters in a Metal-

Organic Framework for Photocatalytic CO_2 Reduction, *Angew. Chem., Int. Ed.*, 2021, **60**, 17388-17393.

19. G. Xu, H. Zhang, J. Wei, H.-X. Zhang, X. Wu, Y. Li, C. Li, J. Zhang and J. Ye, Integrating the g-C_3N_4 Nanosheet with B–H Bonding Decorated Metal–Organic Framework for CO_2 Activation and Photoreduction, *ACS Nano*, 2018, **12**, 5333-5340.

20. M. H. Ye, X. Wang, E. Z. Liu, J. H. Ye and D. F. Wang, Boosting the Photocatalytic Activity of P25 for Carbon Dioxide Reduction by using a Surface-Alkalinized Titanium Carbide MXene as Cocatalyst, *ChemSusChem*, 2018, **11**, 1606-1611.